

Constraining the X-ray AGN halo occupation distribution: implications for eROSITA

Priyanka Singh¹ ^{*}, Alexandre Refregier², Subhabrata Majumdar³ and Biman B. Nath¹

¹ *Raman Research Institute, Bangalore 560080, India*

² *Institute for Astronomy, Department of Physics, ETH Zürich, Wolfgang-Pauli-Strasse 27, CH-8093 Zürich, Switzerland*

³ *Tata Institute of Fundamental Research, Mumbai 400005, India*

14 September 2018

ABSTRACT

The X-ray emission from active galactic nucleus (AGN) is a major component of extragalactic X-ray sky. In this paper, we use the X-ray luminosity function (XLF) and halo occupation distribution (HOD) formalism to construct a halo model for the X-ray emission from AGNs. Verifying that the two inputs (XLF and HOD) are in agreement with each other, we compute the auto-correlation power spectrum in the soft X-ray band (0.5–2 keV) due to the AGNs potentially resolved by eROSITA (extended ROentgen Survey with an Imaging Telescope Array) mission and explore the redshift and mass dependence of the power spectrum. Studying the relative contribution of the Poisson and the clustering terms to the total power, we find that at multipoles $l \lesssim 1000$ (i.e. large scales), the clustering term is larger than the Poisson term. We also forecast the potential of X-ray auto-correlation power spectrum and X-ray-lensing cross-correlation power spectrum using eROSITA and eROSITA-LSST (Large Synoptic Survey Telescope) surveys, respectively, to constrain the HOD parameters and their redshift evolution. In addition, we compute the power spectrum of the AGNs lying below the flux resolution limit of eROSITA, which is essential to understand in order to extract the X-ray signal from the hot diffuse gas present in galaxies and clusters.

Key words: galaxies: nuclei large-scale structure of Universe X-rays: galaxies.

1 Introduction

Almost every galaxy with a central bulge contains a supermassive black hole (SMBH) ($M_{\text{SMBH}} \gtrsim 10^6 M_{\odot}$) at its centre (Kormendy & Richstone 1995; Ferrarese & Merritt 2000). The SMBH acquires a large mass through accretion of matter from its surrounding and the merger of the host galaxies. These processes trigger the active galactic nucleus (AGN) phase of the SMBH during which the accretion rates are high and the accreting material emits a large fraction of its rest energy. The luminosity of the AGN may surpass the total light from the galaxy and drive strong galactic outflows. The evidence of such a feedback from the AGN is present in massive galaxies, groups and clusters. Simulations (Omnia et al. 2004; Springel, Di Matteo & Hernquist 2005; McNamara & Nulsen 2007; Puchwein, Sijacki & Springel 2008; Battaglia et al. 2010; McCarthy et al. 2010) as well as analytical studies (Valageas & Silk 1999; Bower et al. 2001; Cavaliere, Lapi & Menci 2002; Sharma & Nath 2013) show that, in the absence of any AGN feedback, it is dif-

ficult to reproduce various observations such as the gas mass fractions, X-ray luminosity scaling relations, heating of cooling flows of galaxy clusters and gas pressure profiles. The cluster gas entropy also holds key to AGN feedback, which can be directly linked to the non-gravitational energy deposited and remaining in the intra-cluster medium (ICM; Chaudhuri, Nath & Majumdar 2012; Chaudhuri, Majumdar & Nath 2013; Iqbal et al. 2016). These studies give indirect but strong evidence of the presence of AGN and support the importance of AGN driven feedback in the evolution of galaxies.

In addition to giving rise to the outflows, AGNs are strong X-rays emitters and form a dominant part of the extragalactic X-ray sky. eROSITA (extended ROentgen Survey with an Imaging Telescope Array) which is a future X-ray satellite with all sky coverage, will provide a large sample of X-ray AGNs (Merloni et al. 2012; Kolodzig et al. 2013a). It will also cover a significant range of angular scales due to its large sky coverage and improved angular resolution ($\sim 30''$ in 0.5–2 keV band) compared to ROSAT all-sky survey, which was the last all-sky X-ray survey with mean point spread function $\sim 2'$ (La Barbera et al. 2009).

* priyankas@rri.res.in

In this paper, we first compute the angular auto-correlation power spectrum of the X-ray emission coming from AGNs, that are expected to be resolved by eROSITA survey, using a halo model approach. There are two main ingredients of this approach. (1) A model that describes the X-ray emission from AGNs. It can be obtained using the X-ray luminosity function (XLF) of AGNs which represents the luminosity distribution of AGNs as a function of redshift. Here we use the XLF given in Aird et al. 2015 (hereafter A15). (2) We also need a model that describes how AGNs populate dark matter haloes (DMH). Large efforts have been invested into probing how the DMH affect the distribution and energetics of AGNs (Croom et al. 2004; Gilli et al. 2005; Krumpel et al. 2012; White et al. 2012; Koutoulidis et al. 2013; Mountrichas et al. 2013; Allevalo et al. 2014; Gatti et al. 2016). The clustering measurements of X-ray AGNs suggest that AGNs occupy haloes in the mass range $\sim 10^{12.5} - 10^{13.5} h^{-1} M_{\odot}$ (Coil et al. 2009; Cappelluti et al. 2010; Allevalo et al. 2011; Leauthaud et al. 2015). AGN clustering measurements can also be used to construct the halo occupation distribution (HOD) model of AGNs (Miyaji et al. 2011; Allevalo et al. 2012; Richardson et al. 2013, hereafter R13). In this formalism, the number of AGN (central+satellite) is modelled in terms of the mass of the host DMH. The HOD analysis describes how AGNs populate the DMH, which can be used to construct the AGN power spectrum. Specifically, we use the HOD model described in R13. This HOD model, however, lacks a redshift dependence, which is expected from the redshift dependence of AGN XLF and the host halo properties. Here, we study the constraints that can be put on the redshift evolution of the HOD model with eROSITA and Large Synoptic Survey Telescope (LSST, LSST Science Collaboration et al. 2009) using the X-ray auto-correlation power spectrum and X-ray-lensing cross-correlation power spectrum of the resolved AGN. The choice of the X-ray-lensing cross-correlation power spectrum is motivated by the fact that the HOD formalism connects the distribution of the AGNs with the host DMH mass and lensing signal is direct tracer of the mass.

Other important components of the X-ray sky are X-ray binaries, the hot gas present in our own Galaxy and the extragalactic hot gas. Amongst these X-ray sources, the large hot gas reservoir ($T_{\text{vir}} \sim 10^7 K$) filling the space between the galaxies in the clusters, known as the ICM, has been observed in its X-ray emission for a long time (Reichert et al. 1981; Jones & Forman 1984; Branduardi-Raymont et al. 1985; Oukbir, Bartlett & Blanchard 1997; Diego, Silk & Sliwa 2003; Diego et al. 2003; Cavagnolo et al. 2009; Hurier et al. 2015). However, the hot gas ($T_{\text{vir}} > 10^6 K$) present in the form of circumgalactic medium (CGM) in massive galaxies ($M_h \sim 10^{12} - 10^{13} h^{-1} M_{\odot}$; Birnboim & Dekel 2003; Kereš et al. 2005; Singh et al. 2015) is less explored in X-rays due to its fainter X-ray emission. Some of the recent observations and studies (Grcevich & Putman 2009; Anderson & Bregman 2011; Dai et al. 2012; Anderson, Bregman & Dai 2013; Bogdán et al. 2013b,a; Putman, Peek & Joung 2012; Gatto et al. 2013) indicate that the CGM can account for a good fraction of the baryons in these galaxies. The X-ray emission from the CGM, therefore, is a promising tool to put strong con-

straints on the distribution and energetics of the gas (Singh et al. 2016) with eROSITA. At energies above 2 keV, the extragalactic point sources like AGN completely dominate the X-ray sky (Lehmann et al. 2001; Kim et al. 2007). Even below 2 keV, where the X-ray emission from the hot gas in the ICM and CGM is significant, the major contribution to the observed X-ray sky comes from AGNs (Soltan 2007). Therefore, studying the X-ray emission from the AGN is crucial to understand the origin and evolution of the AGN as well as to extract the X-ray signal from the subdominant components. We thus also compute the angular power spectrum of the unresolved AGNs which are expected to contribute to the diffuse X-ray background of eROSITA and contaminate the angular power spectrum due the ICM/CGM in the 0.5-2 keV X-ray band.

This paper is organised as follows. In section-2, we describe the methodology and various ingredients required for the calculation of X-ray power spectrum from the resolved AGNs, and show the redshift and halo mass dependence of the power spectrum. In section-3, we forecast the constraints on the HOD parameters and their redshift evolution. In section-4, we describe the X-ray-lensing cross-power spectrum and its power to put stringent constraints on HOD model parameters. In section-5, we compute the X-ray auto-correlation power spectrum due to the unresolved AGNs, its redshift and halo mass dependence. Finally, we summarise our main conclusions in section-6. The cosmological parameters used in this paper are taken from Planck Collaboration et al. (2016).

2 Auto-correlation power spectrum of the resolved AGNs

Given a signal $x(\theta, \phi)$, its angular power spectrum is given by (eg. Hivon et al. 2002; Molinari et al. 2014),

$$C_l = \frac{1}{2l+1} \sum_{m=-l}^{m=l} |a_{lm}|^2 \quad (1)$$

where, $a_{lm} = \int d\Omega x(\theta, \phi) w(\theta, \phi) Y_{lm}^*(\theta, \phi)$, $w(\theta, \phi)$ is the mask (decided by the sky coverage of the survey with low foreground and low instrumental noise) and Y_{lm}^* are the spherical harmonic functions. There are also other corrections applied to the above power spectrum due to the partial sky coverage of the survey, which is generally the case.

Presently, due to the small sky coverage of the ongoing X-ray surveys, the clustering of AGNs are usually studied only through their two-point correlation function (2PCF). But, with the launch of eROSITA, it will be possible to explore the power spectrum of these AGNs in great detail. Therefore, we choose to deal with the number-weighted power spectrum of AGNs that are expected to be resolved by eROSITA i.e. AGNs lying above the flux resolution limit of eROSITA. We assume that all AGNs above the flux limits $\sim 1.5 \times 10^{-14}$ and $1.8 \times 10^{-13} \text{erg s}^{-1} \text{cm}^{-2}$ in 0.5-2 keV (soft) and 2-10 keV (hard) X-ray bands, respectively, will be resolved by eROSITA.

For resolved AGNs, $x(\theta, \phi)$ represents the AGN number counts, whereas in the case of unresolved AGNs, it represents unresolved X-ray flux. In reality, the observed signal also contains contribution from many other sources and one

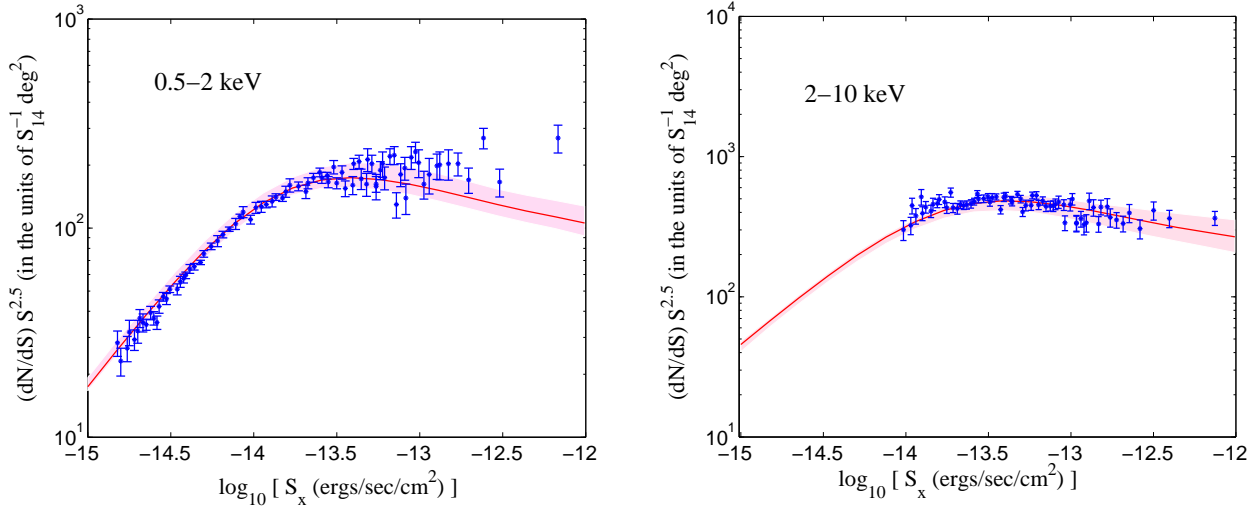


Figure 1. The observed differential number counts of X-ray AGNs (blue points with error bars) from Mateos et al. (2008) against the prediction of the XLF (solid red line) in the soft (left-hand panel) and the hard (right-hand panel) X-ray bands. In both the panels, the shaded region represents the $3\text{-}\sigma$ uncertainty in the prediction of the XLF.

has to carefully remove the noise to get the desired power spectrum. In this paper, we show the analytical estimate of the angular power spectrum calculated using halo model approach. In this approach, the AGN power spectrum is represented by the total contribution of the AGNs residing in a halo, convolved with the DMH mass function, integrated over mass and redshift, as a function of multipole l . The AGN angular auto-correlation power spectrum is the sum of two terms,

$$C_l^{\text{AGN}} = C_l^{\text{AGN,P}} + C_l^{\text{AGN,C}} \quad (2)$$

where $C_l^{\text{AGN,P}}$ and $C_l^{\text{AGN,C}}$ are the Poisson and clustering terms, respectively.

2.1 Poisson term

The Poisson term (independent of l ; also known as shot noise) of the AGN angular auto-correlation power spectrum is given by

$$C_P^{\text{AGN}} = \int dz \frac{dV}{dz d\Omega} \int d \log L_X \phi_{\text{AGN}}(L_X, z) \quad (3)$$

The above equation also represents the number of AGNs per unit solid angle. Here $\phi_{\text{AGN}}(L_X, z)$ is the XLF and L_X is the X-ray luminosity of the AGN (in the hard X-ray band) related to the observed X-ray flux (in the soft X-ray band) S_X by,

$$L_X = \frac{4\pi d_L^2(z) S_X}{(1+z)^{2-\Gamma}} \frac{E_{\text{max,RF}}^{2-\Gamma} - E_{\text{min,RF}}^{2-\Gamma}}{E_{\text{max,obs}}^{2-\Gamma} - E_{\text{min,obs}}^{2-\Gamma}} \quad (4)$$

where $d_L(z)$ is the luminosity distance, Γ is the AGN spectral index (assuming that the AGN X-ray emission follows a power law spectrum), $E_{\text{max,RF}}$ and $E_{\text{min,RF}}$ are the upper and lower limit of the X-ray band in the rest frame of the AGN, respectively, whereas, $E_{\text{max,obs}}$ and $E_{\text{min,obs}}$

correspond to the observed X-ray band. The lower luminosity limit in above integral is determined by the sensitivity limit of the telescopes, which is $\sim 1.5 \times 10^{-14} \text{ erg s}^{-1} \text{ cm}^{-2}$ and $1.8 \times 10^{-13} \text{ erg s}^{-1} \text{ cm}^{-2}$ for soft and hard X-ray bands, respectively.

2.2 AGN XLF

The AGN XLF is defined as the comoving number density of AGNs per unit logarithmic X-ray luminosity, i.e. $\phi_{\text{AGN}}(L_X, z) = dn/d \log_{10} L_X$. To compute it, we use the Luminosity And Density Evolution (LADE) model (see A15 for the details of the model), which gives

$$\phi_{\text{AGN}}(L_X, z) = K(z) \left[\left(\frac{L_X}{L_*(z)} \right)^{\gamma_1} + \left(\frac{L_X}{L_*(z)} \right)^{\gamma_2} \right]^{-1}, \quad (5)$$

where $K(z) = K_0 \times 10^{d(1+z)}$ and $L_*(z) = L_0 \left[\left(\frac{1+z_c}{1+z} \right)^{p_1} + \left(\frac{1+z_c}{1+z} \right)^{p_2} \right]^{-1}$. The values of the model parameters are shown in table-1. Note that this XLF corresponds to luminosities integrated in the hard X-ray band in the rest frame of the AGN. Therefore, one has to take into account the band correction (see equation-4) to estimate the XLF in different X-ray bands.

The differential number counts i.e. the number of AGNs per unit flux and solid angle in the soft band is

$$\frac{dN}{dS_X d\Omega} = \frac{1}{S_X \ln 10} \int dz \frac{dV}{dz d\Omega} \phi_{\text{AGN}}(L_X, z), \quad (6)$$

where $dV/dz d\Omega$ is the differential comoving volume. We compare the AGN differential number counts calculated using the LADE model with the observed number counts (Mateos et al. 2008) for soft as well as hard X-ray band in figure-1. We take $\Gamma = 1.7$ for soft and 2.0 for the hard X-ray band. There is a good agreement between the observed AGN counts and the LADE model.

In figure-2, we show the redshift distribution of AGNs that are expected to be observed by eROSITA in the soft as

Table 1. LADE model parameters.

Parameter	Soft X-ray band	Hard X-ray band
$\log K_0(\text{Mpc}^{-3})$	-4.28	-4.03
$\log L_0(\text{erg s}^{-1})$	44.93	44.84
γ_1	0.44	0.48
γ_2	2.18	2.27
p_1	3.39	3.87
p_2	-3.58	-2.12
z_c	2.31	2.00
d	-0.22	-0.19

well as the hard X-ray band. The soft and hard band AGN number counts get maximum contribution from AGNs near $z \sim 1.2$ and 0.2 , respectively. The hard band AGNs are less concentrated near the peak than the soft band AGNs with a hint of another peak near $z \sim 1.2$. Beyond $z \sim 4$, the number of resolved AGNs becomes negligible.

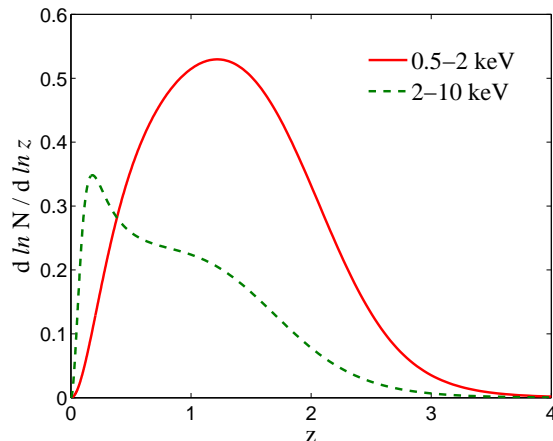
In figure-3, we show the luminosity distribution of the resolved AGNs in the soft and hard X-ray bands. In the soft band, the luminosity distribution peaks at $L_X \sim 10^{44.5} \text{erg s}^{-1}$. In the hard band, the peak is at smaller X-ray luminosity, $L_X \sim 10^{43.4} \text{erg s}^{-1}$. Again, the hard X-ray AGNs have a much broader luminosity distribution compared to the soft X-ray AGNs. In both the bands, negligible fraction of the total resolved AGN population lies outside the luminosity range $L_X \sim 10^{41} - 10^{47} \text{erg s}^{-1}$.

Note that, the prediction of redshift and luminosity dependence of the AGNs crucially depend on the choice of the XLF. Different XLFs, though broadly consistent with each other, give rise to different shapes and peak values of the AGN redshift and luminosity distributions (see figure-10 of Kolodzig et al. 2013b). Also, our default XLF (A15) describes the AGN in 2-10 keV rest frame and for simplicity we use the power law approximation to get the soft band XLF, neglecting the effect of evolving fraction of absorbed and unabsorbed AGNs, which may affect the overall redshift distribution of the AGNs. Our choice of XLF is motivated by the reasonable reproduction of AGN number counts (shown in figure-1) and its consistency with the HOD model used in this paper (discussed later in section-2.3.1). We have also found a good agreement between the predictions of redshift distribution of the soft band AGNs using A15 and Ebrero et al. (2009) XLFs, where the authors use the luminosity function for the 0.5-2 keV observed band. The luminosity distribution of the soft band AGNs estimated using A15 is more consistent with the prediction of AGN XLF by Miyaji, Hasinger & Schmidt (2000). The possible reasons for the disagreement between various AGN XLFs are described in detail in section-5.3 of Kolodzig et al. (2013b).

2.3 Clustering term

The clustering term of the AGN angular auto-correlation power spectrum can be further divided into two terms (Mo, van den Bosch & White 2010; Miyaji et al. 2011; Helgason et al. 2014),

$$C_l^{\text{AGN,C}} = C_l^{\text{AGN,1h}} + C_l^{\text{AGN,2h}}, \quad (7)$$

**Figure 2.** The differential redshift distribution of the AGNs expected to be resolved by eROSITA all-sky survey in the soft (solid red line) and the hard (dashed green line) X-ray bands.**Table 2.** Parameters of MOF.

Parameter	Best fitting value
$\log(M_{\text{min}}/h^{-1}M_{\odot})$	13.65
$\sigma_{\log M}$	0.78
$\log(M_1/h^{-1}M_{\odot})$	14.32
α	2.59
$\log(M_{\text{cut}}/h^{-1}M_{\odot})$	11.0

where $C_l^{\text{AGN,1h}}$ is due to the correlation between AGNs within the same halo and $C_l^{\text{AGN,2h}}$ is due to the correlation between AGNs residing in different haloes.

2.3.1 Two-halo clustering term

The contribution of clustering term to the AGN angular auto-correlation power spectrum due to the correlation between AGNs residing in different haloes (under flat sky approximation) is

$$C_l^{\text{AGN,2h}} = \int dz \frac{dV}{dz d\Omega} P_{\text{AGN}}^{2h} \left(k = \frac{l}{\chi(z)} \right) [W^{\text{AGN}}(z)]^2 \quad (8)$$

where $\chi(z)$ is the comoving distance,

$$P_{\text{AGN}}^{2h}(k) \approx P_{\text{lin}}(k) \left[\int dM \frac{dn}{dM} b_h(M, Z) \times \left(\frac{\langle N_c(M) \rangle + \langle N_s(M) \rangle f_{\text{AGN}}(k, M, z)}{\bar{n}_{\text{AGN}}} \right) \right]^2 \quad (9)$$

and

$$W^{\text{AGN}}(z) = \int d \log L_x \phi_{\text{AGN}}(L_x) \quad (10)$$

where $P_{\text{lin}}(k)$ is the linear matter power spectrum, $b_h(M, z)$ is the linear bias parameter, \bar{n}_{AGN} is the average comoving number density of the AGNs, $\langle N_c(M) \rangle$ and $\langle N_s(M) \rangle$ are the average numbers of central and satellite AGN residing in a halo of mass M , respectively, and $f_{\text{AGN}}(k, M, z)$ [defined such that, $f_{\text{AGN}}(k, M, z) \rightarrow 1$ at large scales] is the Fourier transform of the normalized AGN distribution

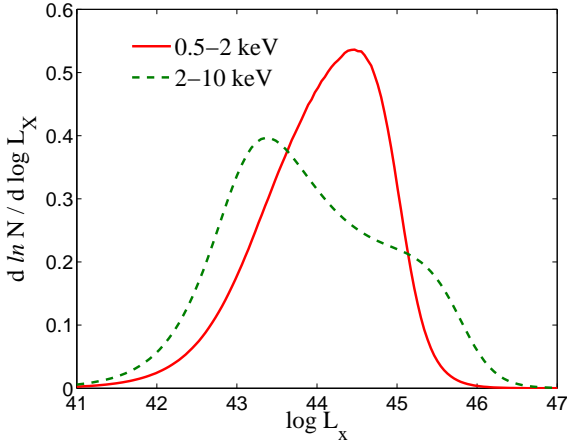


Figure 3. Same as figure-2 but for the luminosity distribution of the resolved AGNs.

within a halo and it is given by,

$$f_{\text{AGN}}(k, M, z) = \int dr 4\pi r^2 n_{\text{AGN}}(r) \frac{\sin(kr)}{kr} \quad (11)$$

where $n_{\text{AGN}}(r)$ is the radial distribution of the satellite AGN, normalized such that its volume integral within the virial radius of the halo is unity. In figure-4, we show $n_{\text{AGN}}(r)$ for $M_h = 10^{14} h^{-1} M_\odot$ at $z = 0$ which is assumed to be given by the Navarro-Frenk-White (NFW) profile (Navarro, Frenk & White 1997) with a concentration parameter (R13 and references therein),

$$c_{\text{AGN}}(M, z) = \frac{32}{(1+z)} \left(\frac{M}{M_{\text{ch}}} \right)^{-0.13} \quad (12)$$

where M_{ch} is a characteristic mass at $z=0$, defined such that $\sigma(M_{\text{ch}}) = 1.686$, where $\sigma(M)$ is the present day smoothed variance of density fluctuations. In the same figure, we also show the NFW profile (with concentration parameter from Duffy et al. 2008), which describes the radial distribution of the dark matter. Due to the high concentration of the AGNs, the radial distribution profile of the AGNs appears steeper than the NFW profile.

Our calculation of the two-halo term does not take into account the effect of scale-dependent bias. Also, if the separation between two objects is less than the sum of the virial radii of their host haloes, they should not be counted in the two-halo term. We neglect this effect, which results in the overestimation of the two-halo term at the scale corresponding to the virial radius of the host halo. However, these corrections are expected to be significant only at small scales (\sim virial size of the object), where one-halo term becomes more important. Therefore, neglecting this effect is not expected to make much difference to our analysis. These corrections are described in detail in Tinker et al. (2005), Zheng et al. (2009), and van den Bosch et al. (2013) for the real space correlation function.

We use the mean occupation function (MOF) i.e. the number of AGNs ($\langle N(M) \rangle$) residing in a halo of mass M from R13, where the authors use the measurement of 2PCF of X-ray selected AGNs by Allevalo et al. (2011) to deter-

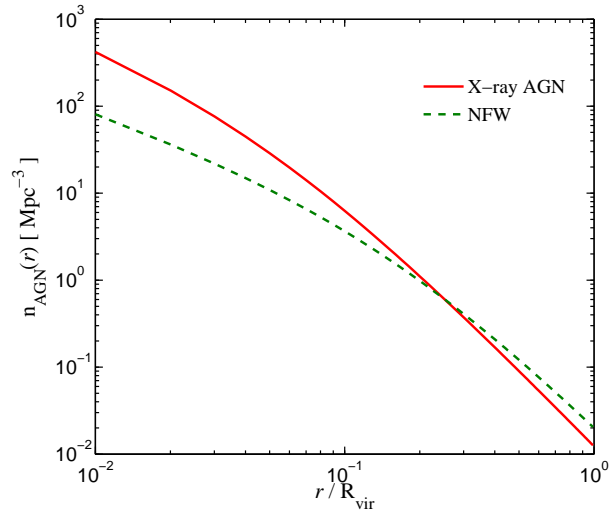


Figure 4. The normalized radial distribution of the X-ray AGNs (solid red line) with concentration parameter given by equation-12, compared with the NFW profile (dashed green line) with concentration parameter from Duffy et al. (2008), for a halo mass $M_h = 10^{14} h^{-1} M_\odot$ at $z = 0$.

mine the HOD parameters.

$$\langle N(M) \rangle = \frac{1}{2} \left[1 + \text{erf} \left(\frac{\log M - \log M_{\text{min}}}{\sigma_{\log M}} \right) \right] + \left(\frac{M}{M_1} \right)^\alpha \exp \left(-\frac{M_{\text{cut}}}{M} \right) \quad (13)$$

where erf is the error function, M_{min} , $\sigma_{\log M}$, M_1 , α and M_{cut} are the model parameters and their values are shown in table-2. The first part of equation-13 represents the central AGN contribution, $\langle N_c(M) \rangle$ and the second part represents the satellite contribution, $\langle N_s(M) \rangle$. At low halo masses ($M_h < 10^{13.5} h^{-1} M_\odot$), the MOF is dominated by the central AGNs, whereas, at high masses ($M_h > 10^{13.5} h^{-1} M_\odot$), the satellite component takes over. In the high mass regime, the number of satellite AGNs is approximately $\propto M^{5/2}$.

In figure-5, we show the mean number density of AGNs calculated using the MOF from R13 ($\bar{n}_{\text{AGN}} = \int dM \langle N(M) \rangle \frac{dn}{dM}$) and the XLF from A15 ($\bar{n}_{\text{AGN}} = \int d \log L_X \phi_{\text{AGN}}(L_X)$) as a function of redshift, confirming that there is a good agreement between the two approaches, especially in the redshift range 0.5-3. Note that we choose the HOD model by R13 over other models for the X-ray AGNs (Miyaji et al. 2011; Allevalo et al. 2012) as the X-ray AGN sample used by R13 span a much wider redshift range compared to that by Miyaji et al. (2011) ($0.16 < z < 0.36$) and Allevalo et al. (2012) ($z \lesssim 1$) and is thus easier to use with the luminosity function considered in this paper.

2.3.2 One-halo clustering term

The contribution of the clustering term to the AGN angular auto-correlation power spectrum due to the correlation between AGNs residing in the same halo can be obtained by replacing $P_{\text{AGN}}^{2h}(k)$ by $P_{\text{AGN}}^{1h}(k)$ in equation-8, with

$$P_{\text{AGN}}^{1h}(k) = \int dM \frac{dn}{dM} \frac{\langle N(M) \rangle (N(M) - 1)}{\bar{n}_{\text{AGN}}^2} f_{\text{AGN}}^2(k) \quad (14)$$

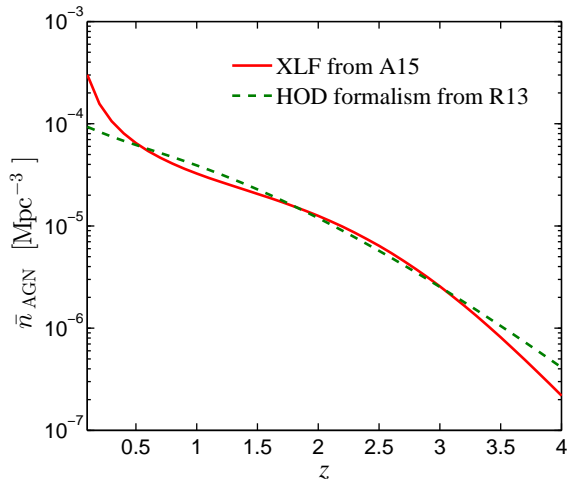


Figure 5. Comparison between the X-ray AGN number density in the soft band as a function of redshift estimated using the XLF from A15 (solid red line) and the HOD formalism from R13 (dashed green line).

Equation-14 assumes that all AGNs residing in a halo follow the same radial profile (Mo, Mao & White 1998). However, the central AGN is located near the centre of the halo and the satellite AGNs are assumed to follow the radial distribution shown figure-4. Taking into account the different distributions of central and satellite AGNs we get

$$P_{\text{AGN}}^{1h}(k) = P_{\text{AGN}}^{1h,ss}(k) + P_{\text{AGN}}^{1h,cs}(k) \quad (15)$$

where $P_{\text{AGN}}^{1h,ss}(k)$ and $P_{\text{AGN}}^{1h,cs}(k)$ are the terms due to satellite-satellite and central-satellite correlation[†], respectively.

$$P_{\text{AGN}}^{1h,ss}(k) = \int dM \frac{dn}{dM} \frac{\langle N_s(M) \rangle^2}{\bar{n}_{\text{AGN}}^2} f_{\text{AGN}}^2(k) \quad (16)$$

$$P_{\text{AGN}}^{1h,cs}(k) = \int dM \frac{dn}{dM} \frac{2\langle N_c(M) \rangle \langle N_s(M) \rangle}{\bar{n}_{\text{AGN}}^2} f_{\text{AGN}}(k) \quad (17)$$

Here, we have assumed that the satellites follow Poisson distribution for which $\langle N_s(M) \rangle \langle N_s(M) - 1 \rangle = \langle N_s(M) \rangle^2$.

In figure-6, we show the number-weighted auto-correlation power spectrum of X-ray AGNs. At large l -values ($l > 1000$) i.e. small scales, the Poisson term dominates the total power spectrum. However, at small l -values ($l < 1000$) i.e. large angular scales, the clustering is larger than the Poisson term. Within the clustering term, the one-halo term is always greater than the two-halo term. Both, the one-halo and the two-halo terms increase with increasing l , till $l \sim 500$, beyond which the two-halo term decreases and the one-halo term continues to increase till $l \sim 1000$, remains approximately constant till $l \sim 10000$ and dies down with further increase in l .

2.4 Redshift and mass dependence

We show the redshift dependence of the Poisson, one-halo and two-halo clustering terms of the AGN auto-correlation

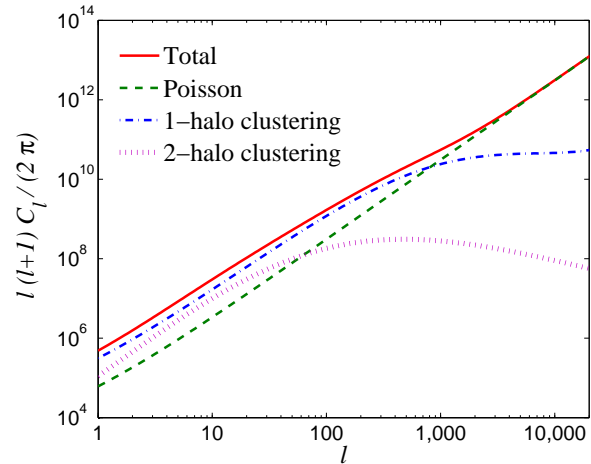


Figure 6. The total power spectrum (solid red line), Poisson term (dashed green line), one-halo (dot-dashed blue line) and two-halo (dotted magenta line) clustering terms due to the resolved AGNs in the soft band.

power spectrum in figure-7. Since, the Poisson term is essentially the number of AGNs, its redshift dependence is identical to the solid red curve in figure-2, with a peak near $z \sim 1.2$. The one-halo clustering term peaks near $z \sim 0.1$ for $l = 10$. Increasing the value of l does not significantly change the redshift corresponding to the peak. Even at $l = 1000$, the power spectrum peaks at $z \sim 0.25$. Therefore, the one-halo clustering term is dominated by low redshifts where the radial structure of the haloes can be probed.

In the case of two-halo clustering term, the power spectrum peaks at $z \sim 0.2, 0.4$ and 1 for $l = 10, 100$ and 1000 , respectively. The two-halo term, comes from the correlation of two distinct haloes, and so depends on the angular difference between two haloes, and hence smaller angular separation (or higher l -value) peaks at higher z . For the one-halo, similar to the two-halo clustering terms, the reason of increasing contribution from high redshift AGN with increasing l value is that the larger l values correspond to smaller angular scales and the distances at higher redshifts appear smaller on the sky.

In figure-8, we show the mass dependence of the AGN clustering terms. The one-halo term peaks near $2 - 3 \times 10^{15} h^{-1} M_{\odot}$ in the l -range $\sim 10 - 1000$ and the peak shifts only slightly to smaller masses with increasing l as smaller objects contribute more at large l . There is negligible contribution coming from low mass haloes ($< 10^{14} h^{-1} M_{\odot}$) to the one-halo term as expected from the AGN MOF. Massive haloes contribute the most due to the large number of satellite AGNs residing in them. However, we note that the mass dependence of the one-halo term is really sensitive to the relation between the satellite AGN MOF and the host halo mass. Since, the average number of satellite AGNs increases rapidly with the halo mass ($\langle N_s(M) \rangle \propto M^{2.59}$), most of the contribution to the power spectrum comes from the high mass end of the galaxy population where the number of galactic haloes decreases exponentially. Also, there is a large uncertainty in the determination of α [hence, in the determination of $\langle N_s(M) \rangle$], as shown in R13. Therefore, the

[†] There is a typo in equation-10 of Miyaji et al. (2011). The first term of the integrand should be $2 \langle N_c N_s \rangle$.

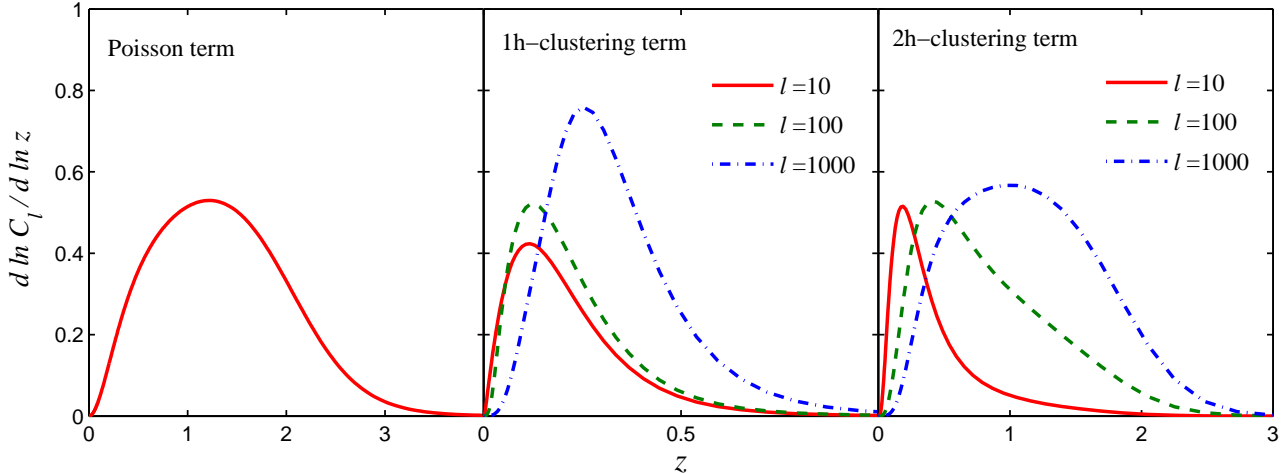


Figure 7. The first, second and third panel show the redshift dependence of the Poisson, one-halo clustering and two-halo clustering terms of the resolved AGN auto-correlation power spectrum in the soft band, respectively. In the case of clustering power spectra, $l = 10, 100$ and 1000 are shown by solid red, dashed green and dot-dashed blue lines, respectively.

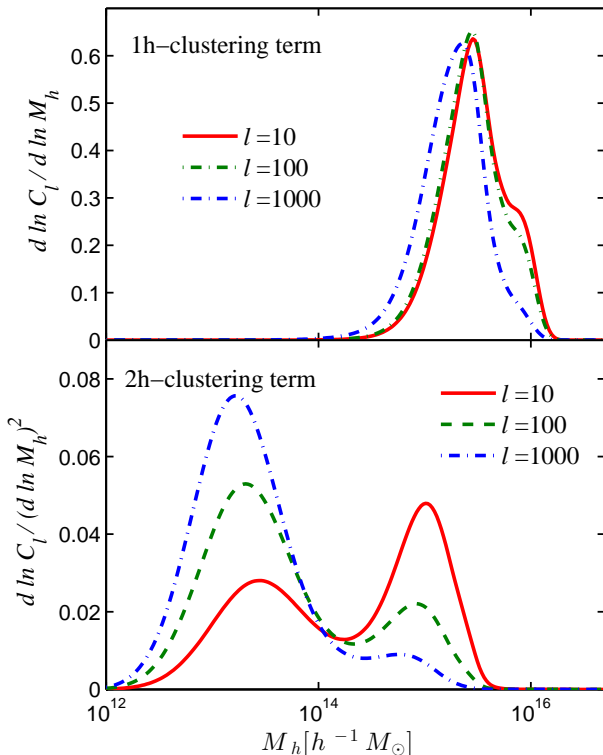


Figure 8. The mass dependence of the one-halo (left-hand panel) and two-halo (right-hand panel) clustering terms of the resolved AGN auto-correlation power spectrum in the soft band. The solid red, dashed green and dot-dashed blue lines corresponds to $l = 10, 100$ and 1000 , respectively.

power spectrum as well as its mass distribution may change significantly with a different value of α .

The two-halo term shows a prominent double peaked structure in its mass distribution due to the different mass

dependences of central and satellite AGNs. The lower mass peak ($\sim 10^{13} h^{-1} M_{\odot}$) comes from the central AGN contribution, whereas, the higher mass peak ($\sim 10^{15} h^{-1} M_{\odot}$) comes from the satellite AGN contribution to the two-halo term. The relative strength of these two peaks depend on the l value. For small l values (i.e. large scales) major contribution comes from the massive haloes, whereas, at large l values (i.e. small scales) the low mass haloes rule the two-halo term. Therefore, at small l , the higher mass peak is more prominent than the smaller mass peak and at large l smaller mass peak overshadows the higher mass peak.

3 Forecast for constraining HOD parameter using auto-correlation power spectrum

There are four free parameters in the AGN HOD model: M_{\min} , $\sigma_{\log M}$, α and M_1 , where M_{\min} is the halo mass at which $\langle N_{\text{cen}} \rangle = 0.5$, $\sigma_{\log M}$ is the width of softened step function used for the central AGN MOF, α is slope of power law relation between the satellite AGN MOF and the halo mass and M_1 is the mass scale at which $\langle N_{\text{sat}} \rangle \approx 1$. The AGN auto-correlation power spectrum can be directly related to the HOD parameters through simple power laws (varying one parameter at a time and keeping all others fixed) in a broad range around the fiducial values of these parameters. For example, C_l has power law dependence on these parameters as follows: $C_l \propto (\log M_{\min})^{1.5}$, $\sigma_{\log M}^{-2}$ and $(\log M_1)^{-4}$ with little to no change in the power law index as a function of l . However, the variation of C_l^{1h} with α cannot be fit by a single power law. The one-halo term has $\langle N_s(M) \rangle^2$ in its integrand and the satellite MOF itself is proportional to $M^{2.59}$. Consequently, the power spectrum is highly biased towards the massive haloes as discussed in section-2.4. However, varying the value of α can significantly alter the power spectrum due to the presence of $\langle N_s(M) \rangle^2$ term. Increasing the value of α results in a large increase in the power spectrum causing the sensitive dependence of the power spectrum on the value of α . For $0.5 < \alpha < 1.5$, $C_l^{1h} \propto \alpha^{1.5(1)}$,

whereas in the range, $1.5 < \alpha < 3.0$, $C_l^{1h} \propto \alpha^{8.7(6.8)}$, at $l = 10(1000)$.

Similarly, C_l^{2h} is proportional to $(\log M_{\min})^{0.5}$ and $\sigma_{\log M}^{-1}$, and the power law indices are nearly independent of l . However, in the case of $\log M_1$, the power law index depends on the fiducial value of M_1 as well as the value of l . At $l = 10$, near the fiducial value of M_1 , $C_l^{2h} \propto (\log M_1)^{-1.1}$. Analogous to the one-halo term, the relation between the two-halo term and α is really sensitive to the value of α as well as l , with $C_l^{2h} \propto \alpha^{0.5(0.3)}$ for $0.5 < \alpha < 2.5$ and $C_l^{2h} \propto \alpha^{2.5(0.6)}$ for $2.5 < \alpha < 3$, at $l = 10(1000)$.

Figure-1-(b) of R13 shows $\langle N_c(M) \rangle$ and $\langle N_s(M) \rangle$ with their 1- σ uncertainties. There is a large uncertainty in $\langle N_c(M) \rangle$ at low halo masses ($M_h < 10^{12.5} h^{-1} M_\odot$) and in $\langle N_s(M) \rangle$ throughout the entire mass range. This is due to the current large uncertainties in the determination of the model parameters, especially for the satellite AGNs. Also, the X-ray AGN sample (Allevato et al. 2011) used to construct the HOD model in R13 spans a broad redshift range (0-4) with a median redshift, $z_{\text{med}} \sim 1.2$. Therefore, this HOD model represents the AGN population at the median redshift, an average over the redshift range of the AGN sample and it lacks any redshift dependence. Other studies (eg. Koutoulidis et al. 2013; Gatti et al. 2016) involving the X-ray AGN clustering measurement also indicate that the HOD may have a weak redshift dependence. However, it is not possible to put strong constraints due to the small sample sizes. In this section, we look into the possibility of constraining the redshift evolution of the HOD model with upcoming eROSITA all-sky survey using a Fisher matrix analysis.

For simplicity, we consider a power law redshift dependence of the parameters. For the purpose of this study, we choose following Fisher parameters:

$$\left\{ \{ \log(M_{\min}), \sigma_{\log M}, \log(M_1), \alpha \}, \{ \gamma_{M_{\min}}, \gamma_{\sigma_{\log M}}, \gamma_{M_1}, \gamma_\alpha \} \right\}, \quad (18)$$

where the power law indices $\gamma_{a,s}$ are defined as,

$$p_a = p_a^{\text{fid}} \left(\frac{1+z}{1+z_{\text{med}}} \right)^{\gamma_a} \quad (19)$$

where, p_a^{fid} s are the fiducial values of the HOD parameters (specified in table-2) and $\gamma_{a,s}$ are the corresponding power law indices. The fiducial values of $\gamma_{a,s}$ are zero i.e. no redshift evolution.

The Fisher matrix can be calculated using,

$$F_{ab} = \Sigma_{ll'} \frac{\partial C_\ell}{\partial p_a} (M_{\ell\ell'})^{-1} \frac{\partial C_{\ell'}}{\partial p_b} \delta_{ll'} \quad (20)$$

where p_a s are the model parameters and $M_{\ell\ell'}$ is the covariance matrix that incorporates the uncertainty in the $C_{l,s}$. $M_{\ell\ell'}$ is given by,

$$M_{\ell\ell'} = \frac{1}{f_{\text{sky}}} \left[\frac{(C_l + N_l)^2 \delta_{\ell\ell'}}{(l + \frac{1}{2}) \Delta l} \right] \quad (21)$$

where f_{sky} is the sky coverage of the survey, N_l is the noise in the power spectrum (we consider AGN shot noise only) and Δl is the l -bin size. For simplicity, we neglect the trispectrum contribution to $M_{\ell\ell'}$ and take $\Delta l = 100$.

We show the forecasted constraints on the parameters in table-3. Note that the no priors, fixed HOD and no redshift evolution cases correspond to no priors on any of the Fisher

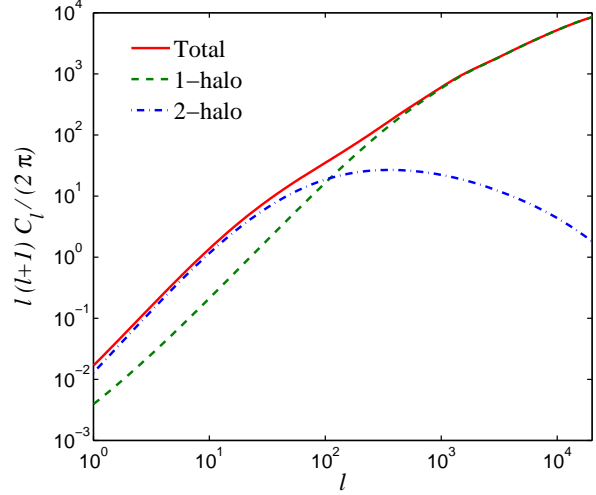


Figure 9. The cross-correlation power spectrum of soft X-ray emission from the AGNs and weak lensing. The total power spectrum, one-halo and two-halo terms are indicated by solid red, dashed green and dot-dashed blue lines, respectively.

parameters, no change in the fiducial values of the HOD parameters and no redshift evolution of the HOD parameters, respectively. Using this method we find that the redshift evolution of the HOD parameters can be constrained to $\Delta \gamma_{M_{\min}} \sim 0.2$, $\Delta \gamma_{\sigma_{\log M}} \sim 3$, $\Delta \gamma_{M_1} \sim 0.02$ and $\Delta \gamma_\alpha \sim 0.03$, with eROSITA and fixed HOD parameters. Since, the AGN power spectrum is more sensitive to the satellite AGNs compared to the central AGN, γ_{M_1} and γ_α are better constrained than $\gamma_{M_{\min}}$, $\gamma_{\sigma_{\log M}}$. Similarly, in the absence of any redshift evolution, the HOD parameters can be constrained to $\Delta \log M_{\min} \sim 1.1$, $\Delta \sigma_{\log M} \sim 0.9$, $\Delta \log M_1 \sim 0.16$ and $\Delta \alpha \sim 0.015$. However, the uncertainties on these parameters crucially depend on the prior information of the model parameters. These constraints degrade significantly if the priors on other parameters are removed as shown in table-3 and one cannot obtain any strong constraint in such a situation.

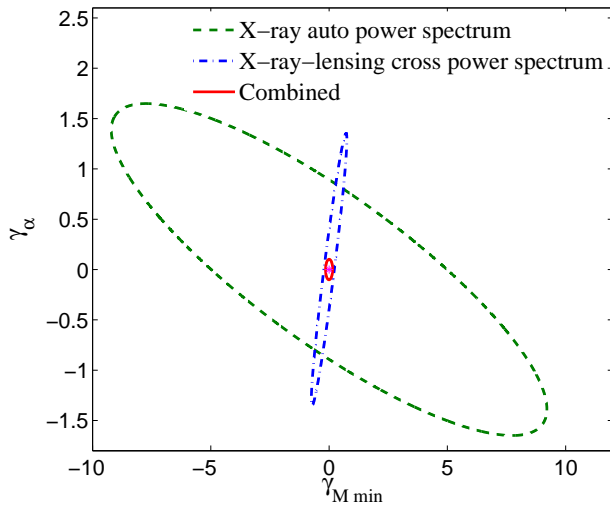
The poor constraints obtained from auto-correlation in the absence of strong priors can be improved by combining the information from different probes of the same parameters. Hence, we compute the cross-correlation power spectrum of X-ray emission from the AGN and the galaxy weak lensing to investigate how this combination can be used to improve the constraints on the HOD parameters.

4 Cross-correlating X-ray AGN with lensing

When the light from a background galaxy is bent by a structure along the line-of-sight, the resulting distortion is known as gravitational lensing. There are two effects of lensing on the image of a background galaxy: convergence (κ), which represents the isotropic stretching of the image, and shear (γ), which represents the anisotropic stretching thus distorting a circular image into an elliptical one. In the weak lensing regime both the convergence and shear are small i.e. $\kappa \ll 1$, $\gamma \ll 1$. The convergence field is a direct probe of the grav-

Table 3. Forecasted constraints on the HOD parameters with eROSITA and eROSITA-LSST combination.

	Power spectrum	$\Delta \log(M_{\min})$	$\Delta \sigma_{\log M}$	$\Delta \log(M_1)$	$\Delta \alpha$	$\Delta \gamma_{M_{\min}}$	$\Delta \gamma_{\sigma_{\log M}}$	$\Delta \gamma_{M_1}$	$\Delta \gamma_{\alpha}$
No priors	X-ray auto	35	23	6	3	6	75	1	1
	X-ray-lensing cross	2.5	1.5	1	1.2	0.5	5.7	0.16	0.9
	Auto+Cross	0.6	0.3	0.17	0.13	0.1	0.9	0.02	0.07
Fixed HOD	X-ray auto	-	-	-	-	0.2	3	0.02	0.03
	X-ray-lensing cross	-	-	-	-	0.1	1	0.03	0.11
	Auto+Cross	-	-	-	-	0.02	0.2	0.004	0.008
No redshift evolution	X-ray auto	1.1	0.9	0.16	0.015	-	-	-	-
	X-ray-lensing cross	0.4	0.2	0.13	0.13	-	-	-	-
	Auto+Cross	0.1	0.06	0.02	0.01	-	-	-	-


Figure 10. The forecasted 68% confidence limit contours for the redshift evolution parameters of the HOD model, $\gamma_{M_{\min}}$ and γ_{α} . The dashed green and dot-dashed blue contours correspond to the constraints due to the X-ray AGN auto and X-ray AGN-galaxy lensing cross-correlation power spectra in the soft band, respectively, whereas, the solid red contour corresponds to the combined auto and cross-correlation power spectra constraints.

itational potential of the lens mass and it can be obtained from the measurement of the shear field. For the detailed procedure of measurement of the shear field and construction of convergence maps see e.g. Refregier (2003), Kilbinger (2015) and references therein.

Cross-correlation of galaxy lensing with other probes such as Sunyaev-Zel'dovich effect (Battaglia, Hill & Murray 2015; Ma et al. 2015), cosmic microwave background lensing (Hand et al. 2015), has been used to understand baryonic physics as well as to put constraints on the cosmological parameters. Since, the motivation of the HOD formalism is to establish a connection between the AGNs and the host halo, cross-correlating X-ray emission from the AGNs and

the lensing signal can provide an additional tool to constrain the HOD model. Therefore, in this section, we estimate the cross-correlation power spectrum of the lensing convergence field with the X-ray emission from AGNs.

4.1 X-ray-lensing cross-correlation power spectrum

Analogous to the X-ray auto-correlation power spectrum, the AGN X-ray-lensing cross-correlation power spectrum in the thin lens limit (i.e. the thickness of the lens is much smaller than the distance between the lens and observer as well as the distance between the lens and source) is given by,

$$C_l^{\text{AGN},\kappa} = \int dz \frac{dV}{dz d\Omega} W_{\text{AGN}}(z) W_{\kappa}(z) P_{\text{AGN},\kappa} \left(k = \frac{l}{\chi(z)} \right) \quad (22)$$

where $W_{\text{AGN}}(z)$ is given by equation-10. The lensing kernel $W_{\kappa}(z)$ for a flat Universe (Van Waerbeke, Hinshaw & Murray 2014) is given by,

$$W_{\kappa}(z) = \frac{3}{2} \Omega_M^0 \left(\frac{H_0}{c} \right)^2 g(z) (1+z) / \chi(z) \quad (23)$$

Here, $g(z)$ is defined as,

$$g(z) = \int_{\chi}^{\chi_H} d\chi' p_s(\chi') \frac{\chi' - \chi}{\chi'} = \int_z^{z_H} dz' p_s(z') \frac{\chi' - \chi}{\chi'} \quad (24)$$

where $p_s(z) = n(z)/n(z=0)$ is the normalized source redshift distribution function. Again, the power spectrum can be decomposed into one-halo and two-halo terms.

$$P_{\text{AGN},\kappa}(k) = P_{\text{AGN},\kappa}^{1h}(k) + P_{\text{AGN},\kappa}^{2h}(k) \quad (25)$$

where,

$$P_{\text{AGN},\kappa}^{1h}(k) = \int dM \frac{dn}{dM} f_{\kappa}(k, M, z) \times \left[\frac{\langle N_c(M) \rangle + \langle N_s(M) \rangle f_{\text{AGN}}(k, M, z)}{\bar{n}_{\text{AGN}}} \right] \quad (26)$$

and

$$P_{\text{AGN},\kappa}^{2h}(k) \approx P_{\text{lin}}(k) \left[\int dM \frac{dn}{dM} b_h(M, Z) f_\kappa(k, M, z) \right] \\ \times \left[\int dM \frac{dn}{dM} b_h(M, Z) \frac{\langle N_c(M) \rangle + \langle N_s(M) \rangle f_{\text{AGN}}(k, M, z)}{\bar{n}_{\text{AGN}}} \right] \quad (27)$$

where, $f_\kappa(k, M, z)$ is the Fourier transform of the dark matter density profile and its given by,

$$f_\kappa(k, M, z) = \int 4\pi r^2 dr \frac{\rho_{\text{DM}}(r)}{\bar{\rho}_M} \frac{\sin(kr)}{kr} \quad (28)$$

where $\rho_{\text{DM}}(r)$ is the NFW density profile and $\bar{\rho}_M$ is the comoving matter density of the universe.

We choose the combination of eROSITA and LSST surveys to forecast the constraints on the HOD model that can be obtained from such a study. The reason of this choice is the high sky coverage of the overlapping region of the two surveys. LSST is a ground based optical telescope, presently under construction. We take the sky coverage of the overlapping region between eROSITA and LSST, $f_{\text{sky}} \sim 0.5$, for the calculation of the covariance matrix. In order to calculate the lensing part, we take the source redshift distribution function, $p_s(z) = (z^3/2z_0^3)e^{-z/z_0}$ (Battaglia, Hill & Murray 2015), where $z_0 = 1/3$ for the LSST survey.

In figure-9, we show the one-halo, two-halo and total X-ray AGN-lensing cross-correlation power spectrum. There is an interesting difference between the X-ray auto-correlation power spectrum and the X-ray-lensing cross-correlation power spectrum. In the case of X-ray auto-correlation power spectrum, two-halo term is always smaller than the one-halo term. But for the cross-correlation power spectrum, on large scales ($l \lesssim 100$), the two-halo term is larger than the one-halo term. This behavior is due to the reason that in the case of galaxy weak lensing auto-correlation power spectrum, the one-halo term becomes larger than the two-halo term at comparatively larger multipoles ($l > 100$, see for example Takada & Bridle 2007). As a result, the X-ray-lensing cross-correlation power spectrum shows the transition from two-halo to one-halo dominance at intermediate multipoles.

4.2 Forecast using the cross-correlation power spectrum

The uncertainty in the X-ray-lensing cross-correlation power spectrum is given by,

$$M_{ll'}^{\text{AGN},\kappa} = \frac{\delta_{ll'}}{f_{\text{sky}}(2l+1)\Delta l} \times \left[\hat{C}_l^{\text{AGN},\text{AGN}} \hat{C}_l^{\kappa\kappa} + \hat{C}_l^{\text{AGN},\kappa} \hat{C}_l^{\kappa,\text{AGN}} \right] \quad (29)$$

where, \hat{C}_l^{ij} s are the auto ($i = j$) or cross ($i \neq j$) power spectra including noise. We consider only the shot noise term to calculate the noise in the X-ray auto-correlation power spectrum, as mentioned in section-3. Noise in the lensing auto-correlation power spectrum is, $N_l^{\kappa\kappa} = \sigma_\gamma^2/n_s$ (Battaglia, Hill & Murray 2015), where, σ_γ and n_s are the intrinsic ellipticity dispersion per component and the 2-dimensional angular number density of the source galaxies, respectively. For LSST, $\sigma_\gamma^2 = 0.28$ and $n_s = 40 \text{ arcmin}^{-2}$. Assuming that the noise in X-ray and lensing surveys are independent of each other, $N_l^{\text{AGN},\kappa} = 0$.

We choose $\gamma_{M_{\text{min}}}$ and γ_α that represent the central and

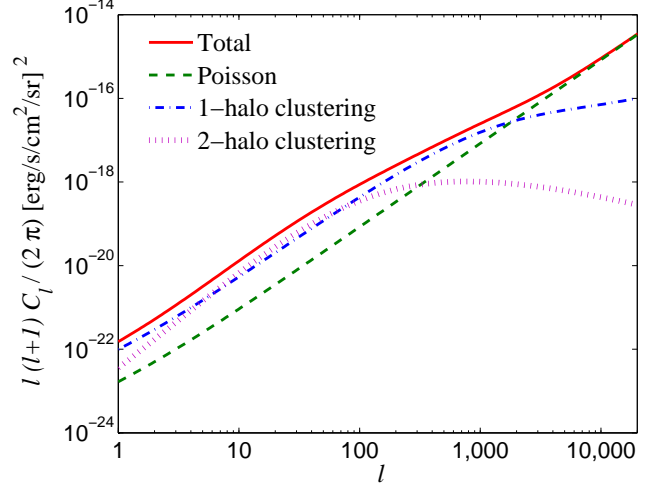


Figure 11. Same as figure-6 but for the unresolved AGNs.

satellite AGNs, respectively, and show the individual as well as the joint constraints on $\gamma_{M_{\text{min}}}$ and γ_α coming from the auto and cross-correlation power spectra in figure-10. Note that, to examine how well these spectra combinations can constrain the model parameters, we do not put any priors on any of the Fisher parameters. The X-ray-lensing cross-correlation analysis can alone constrain $\gamma_{M_{\text{min}}}$ and γ_α to approximately, 0.5 and 0.9, respectively. The uncertainty on $\gamma_{M_{\text{min}}}$ is much better for the cross correlation signal compared to the auto-correlation signal, whereas, the uncertainty on γ_α is similar for the two cases. The reason of the loose constraint on $\gamma_{M_{\text{min}}}$ as compared to γ_α coming from the X-ray auto-correlation power spectrum is that the X-ray auto-correlation power spectrum is much more sensitive to the satellite AGN MOF, hence γ_α in comparison to the central AGN MOF, hence $\gamma_{M_{\text{min}}}$ (see equation-16 and 17). On the contrary, the X-ray-lensing cross-correlation power spectrum has similar dependence on the central as well as satellite AGN MOF (see equation-26), resulting in similar constraints on the corresponding Fisher parameters. In addition, this difference in dependence of the auto and cross-correlation power spectra on the central and satellite terms give rise to distinct directions of degeneracy in $\gamma_{M_{\text{min}}}$ and γ_α uncertainty contours, as shown in figure-10. Consequently, the constraints obtained by combining the X-ray auto and X-ray-lensing cross-correlation power spectra Fisher matrices are much better than their individual constraints. The constraints obtained from the combined as well as individual Fisher matrices are shown in table-3.

5 Unresolved AGNs

Depending on the flux limit of the X-ray survey, a fraction of AGNs may remain unresolved in the X-ray map. These unresolved X-ray AGNs are the prime source of contamination while studying the diffuse X-ray emission from the hot gas in the ICM and CGM. Therefore, modelling the unresolved AGNs appropriately is essential to extract the X-ray emission from the hot gas and hence the gas physics. In

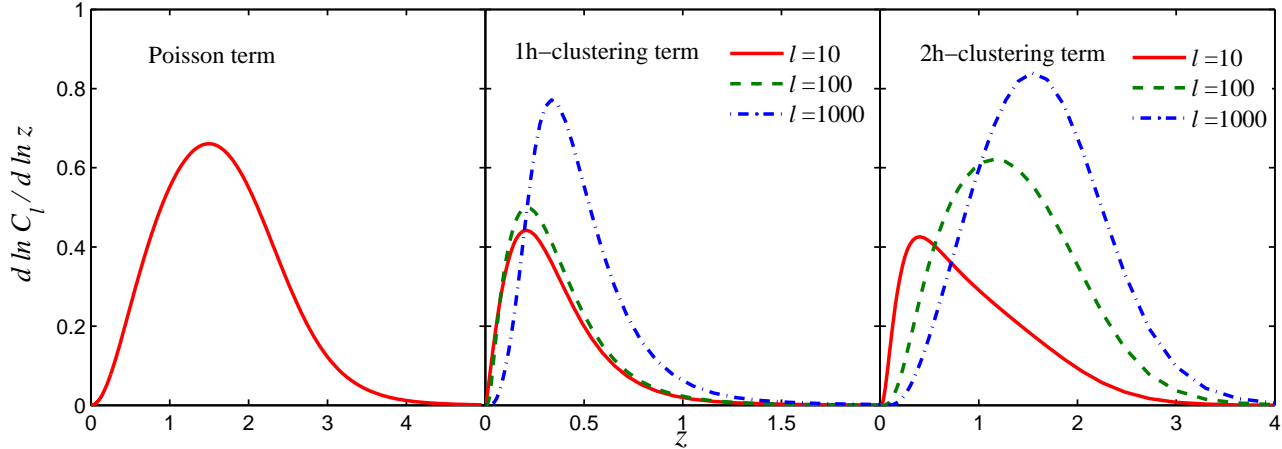


Figure 12. Same as figure-7 but for the unresolved AGNs.

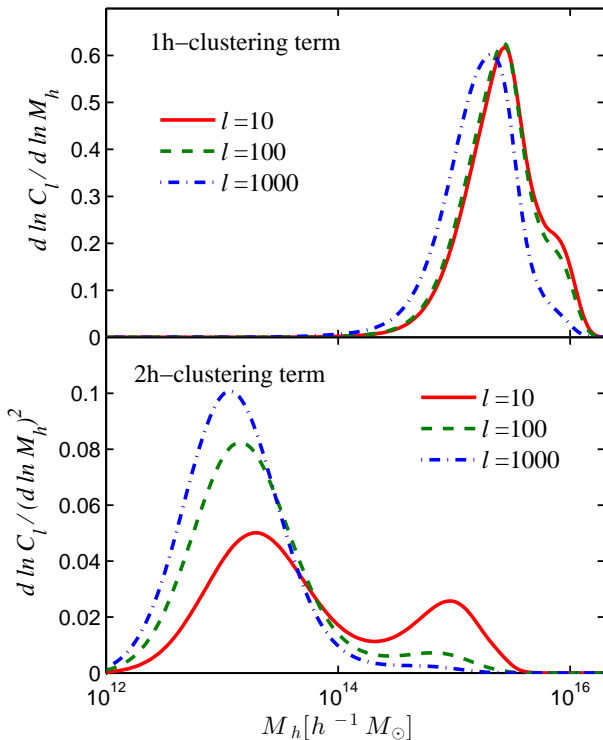


Figure 13. Same as figure-8 but for the unresolved AGNs.

this section, we estimate the flux-weighted angular power spectrum, the redshift and halo mass dependence of the power spectrum for the unresolved AGNs, assuming that these AGNs are also described by the same luminosity function and the HOD model. The reason for the choice of flux-weighted power spectrum is that it is not possible to identify the source of these X-ray photons as their hosts are not resolved by the X-ray telescope, which rules out the number-weighted power spectrum.

5.1 Flux-weighted angular auto-correlation power spectrum

As mentioned in section-2, the estimator of unresolved AGN power spectrum is given by equation-1, where, the signal $x(\theta, \phi)$ is the unresolved X-ray flux. Analogous to the resolved AGNs, the flux-weighted power spectrum of the unresolved AGNs is the sum of Poisson and clustering terms. The Poisson term is given by,

$$C_P^{\text{AGN}} = \int dz \frac{dV}{dz d\Omega} \int d \log L_X \phi_{\text{AGN}}(L_X, z) S_X^2 \quad (30)$$

In contrast to the resolved AGN, the lower luminosity limit in the above integral is set to zero and the upper luminosity limit is fixed by the sensitivity limit of the X-ray telescope for the unresolved AGN.

Again, the clustering term is composed of one-halo and two-halo terms given by equation-14 and 9, respectively, with $W^{\text{AGN}}(z)$ replaced by,

$$W^{\text{AGN}}(z) = \int d \log L_X \phi_{\text{AGN}}(L_X) S_X \quad (31)$$

In figure-11, we show the flux-weighted auto-correlation power spectrum for AGNs lying below the flux resolution limit of eROSITA. Similar to the resolved AGNs, at lower multipoles, the clustering term is dominant whereas at large multipoles, the Poisson term takes over the total power spectrum. However, this takes place near $l \sim 2000$ in the case of unresolved AGNs, compared to $l \sim 1000$ for the resolved AGNs. Another visible difference between the resolved and the unresolved AGN power spectrum is that the two-halo clustering term is always smaller than the one-halo clustering term for the resolved AGN, whereas, the two-halo term is slightly larger than one-halo term in the l -range 10-100 for the unresolved AGNs.

5.2 Redshift and mass dependence

In figure-12, we show the redshift dependence of the Poisson, one-halo clustering and two-halo clustering power spectra of

the unresolved AGNs. The redshift distribution of the unresolved AGN power spectra have small but non-negligible contribution from the higher redshift AGNs compared to the resolved AGNs, with similar shape of the overall distribution. The Poisson term peaks at $z \sim 1.5$. This peak is at slightly higher redshift compared to the redshift distribution of the resolved AGNs (see figure-2) which peaks near $z \sim 1.2$, due to the simple fact that a high redshift AGN with the same luminosity as a low redshift AGNs, corresponds to a lower flux and hence may remain unresolved depending on the telescope's resolution. For the one-halo clustering term, the power spectrum peaks near $z \sim 0.2$, for $l \sim 10$ and the peak shifts only slightly to higher redshifts with increasing value of l .

The two-halo clustering term peaks at $z \sim 0.5$, for $l \sim 10$ and the peak shifts significantly with increasing value of l . For $l \sim 1000$, the two-halo clustering power spectrum is dominated by $z \sim 1.5$ AGNs. Since, the total power spectrum is controlled by clustering term at $l < 2000$ and Poisson term at $l > 2000$, the overall power spectrum is governed by low to intermediate redshift AGNs ($z \sim 0.2-1.5$).

The mass dependence of the unresolved AGN power spectrum is shown in figure-13. The one-halo clustering term of the unresolved and resolved AGNs (figure-8) have almost identical halo mass dependence, with a peak near $10^{15} h^{-1} M_{\odot}$ due to the highly biased MOF of the satellite AGNs towards massive haloes.

The two-halo clustering power spectrum also show a double peaked mass distribution similar to the one observed in case of resolved AGNs. However, the low mass peak ($\sim 10^{13} h^{-1} M_{\odot}$) is more prominent than the high mass peak ($\sim 10^{15} h^{-1} M_{\odot}$), even at $l = 10$. At higher l values, most of the contribution to the two-halo term comes from $10^{12} - 10^{14} h^{-1} M_{\odot}$ haloes.

6 Conclusions

In this work, we divided the AGNs into two categories: 1) resolved AGNs, which lie above the flux resolution limit of eROSITA, and 2) unresolved AGNs, lying below this limit. We computed the number-weighted and flux-weighted angular power spectra for the resolved and unresolved AGNs, respectively, in the soft X-ray band. We used the LADE model for the X-ray AGN luminosity function described in A15 (which matches well with the observed AGN number counts) and the HOD model for the X-ray AGNs by R13, which describe the luminosity distribution and halo mass dependence of the AGNs, respectively. We also calculated the luminosity and redshift dependence of the resolved AGNs finding that the maximum contribution to the AGN luminosity and redshift distribution comes from $L_X \sim 2 - 3 \times 10^{44}$ erg s^{-1} and $z \sim 1.2$, respectively. We computed the number density of the X-ray AGNs using the XLF as well as the HOD formalism and found that the two approaches are in good agreement with each other in a wide range of redshift (especially at $0.5 \lesssim z \lesssim 3.5$). The X-ray auto-correlation power spectrum has the following features.

(i) The power spectrum of the resolved AGNs is dominated by low redshift AGNs ($z \sim 0.1-0.2$) at low multipoles ($l < 1000$) due to the dominant contribution from the one-halo clustering term at these multipoles. However, at large

multipoles ($l > 1000$), where the Poisson term controls the total power spectrum, the redshift dependence of the power spectrum peaks at intermediate redshifts ($z \sim 1.2$). The one-halo term is larger than the two-halo term down to $l = 1$, though at low multipoles these two terms have similar amplitudes.

(ii) For the unresolved AGNs, the power spectrum is dominated by Poisson term and hence $z \sim 1.5$ AGNs at $l > 2000$. In the range $l \sim 100 - 2000$, where the one-halo clustering term is dominant, the total power spectrum is governed by $z \sim 0.2 - 0.3$ AGNs. At $l < 100$, the power spectrum has major contribution from $z < 1$ AGNs due to significant contribution from two-halo as well as the one-halo clustering terms.

(iii) The HOD model that we use in this work predicts a large number of satellite AGNs in massive haloes. This mass dependence shows up in the mass dependence of the AGN power spectrum (resolved as well as unresolved). Both the one-halo and two-halo terms show peaks at the high mass end ($M_h \sim 10^{15} h^{-1} M_{\odot}$) of the DMH. Interestingly, the two-halo term shows an additional peak at lower halo mass ($M_h \sim 10^{13} h^{-1} M_{\odot}$), which is due to the contribution from the central AGN. The low mass peak becomes more prominent than the high mass peak at large multipoles i.e. small angular scales, especially in the case of unresolved AGNs.

We also investigated the role of eROSITA in constraining the redshift evolution of the HOD parameters, which play a crucial role in determining the AGN power spectrum, using the Fisher matrix analysis. We assumed a simple power law dependence of the HOD parameters on the redshift and found that the uncertainties in the determination of these power law indices vary significantly with and without any priors on other HOD parameters. Without any priors, the X-ray auto-correlation power spectrum poorly constrains these parameters (shown in table-3). To improve upon this, we included X-ray-lensing cross-correlation power spectrum, which is motivated by the fact that lensing traces the total halo mass and that the HOD model describes the relation between the host halo mass and AGNs. The cross-correlation power spectrum can alone put much better constraints on the model parameters (except for the satellite AGN parameters in some situations) and combining the auto and cross-correlation power spectra improves the uncertainties further. For example, γ_{M_1} , which describes the redshift evolution of the relation between the satellite AGN MOF and the host halo mass, can be constrained to $\Delta\gamma_{M_1} \sim 1$ and 0.16, using the X-ray auto and X-ray-lensing cross-correlation power spectra, respectively, and the constraint improves to $\Delta\gamma_{M_1} \sim 0.02$ with the auto and cross-correlation power spectra combination, without any prior information on any other parameter. Adding prior information on the Fisher parameters can significantly reduce their uncertainties. The uncertainty on γ_{M_1} coming from the X-ray auto-correlation power spectrum only, reduces to $\Delta\gamma_{M_1} \sim 0.03$, if the uncertainties on the fiducial values of the HOD model parameters are reduced to zero. Other parameters also follow the same trend depending on the sensitivity of the power spectrum considered, with respect to the parameter.

Our power spectrum analysis suggest that the present constraints on the AGN HOD parameters will improve

significantly with the availability of eROSITA and LSST. At the same time, due to the potential of eROSITA to probe the hot gas in galaxies, such an analysis is expected to play a crucial role in separating the contribution from the AGNs and the hot gas.

ACKNOWLEDGEMENTS

We thank the anonymous referee for valuable suggestions and comments. We thank Takamitsu Miyaji, James Aird, Aseem Paranjape, Suchetana Chatterjee and Jonathan Richardson for helpful discussions. We also thank James Aird for providing the results on the uncertainties in the LADE model parameters.

REFERENCES

- Aird J., Coil A. L., Georgakakis A., Nandra K., Barro G., Pérez-González P. G., 2015, *MNRAS*, 451, 1892 (A15)
- Allevato V. et al., 2011, *ApJ*, 736, 99
- Allevato V. et al., 2014, *ApJ*, 796, 4
- Allevato V. et al., 2012, *ApJ*, 758, 47
- Anderson M. E., Bregman J. N., 2011, *ApJ*, 737, 22
- Anderson M. E., Bregman J. N., Dai X., 2013, *ApJ*, 762, 106
- Battaglia N., Bond J. R., Pfrommer C., Sievers J. L., Sijacki D., 2010, *ApJ*, 725, 91
- Battaglia N., Hill J. C., Murray N., 2015, *ApJ*, 812, 154
- Birnboim Y., Dekel A., 2003, *MNRAS*, 345, 349
- Bogdán Á., Forman W. R., Kraft R. P., Jones C., 2013a, *ApJ*, 772, 98
- Bogdán Á. et al., 2013b, *ApJ*, 772, 97
- Bower R. G., Benson A. J., Lacey C. G., Baugh C. M., Cole S., Frenk C. S., 2001, *MNRAS*, 325, 497
- Branduardi-Raymont G., Kellett B., Fabian A. C., McGlynn T., Manzo G., 1985, *Advances in Space Research*, 5, 133
- Cappelluti N., Ajello M., Burlon D., Krumpke M., Miyaji T., Bonoli S., Greiner J., 2010, *ApJ*, 716, L209
- Cavagnolo K. W., Donahue M., Voit G. M., Sun M., 2009, *ApJS*, 182, 12
- Cavaliere A., Lapi A., Menci N., 2002, *ApJ*, 581, L1
- Chaudhuri A., Majumdar S., Nath B. B., 2013, *ApJ*, 776, 84
- Chaudhuri A., Nath B. B., Majumdar S., 2012, *ApJ*, 759, 87
- Coil A. L. et al., 2009, *ApJ*, 701, 1484
- Croom S. et al., 2004, in *Astronomical Society of the Pacific Conference Series*, Vol. 311, *AGN Physics with the Sloan Digital Sky Survey*, Richards G. T., Hall P. B., eds., p. 457
- Dai X., Anderson M. E., Bregman J. N., Miller J. M., 2012, *ApJ*, 755, 107
- Diego J. M., Silk J., Sliwa W., 2003, *MNRAS*, 346, 940
- Diego J. M., Sliwa W., Silk J., Barcons X., 2003, *MNRAS*, 344, 951
- Duffy A. R., Battye R. A., Davies R. D., Moss A., Wilkinson P. N., 2008, *MNRAS*, 383, 150
- Ebrero J. et al., 2009, *A&A*, 493, 55
- Ferrarese L., Merritt D., 2000, *ApJ*, 539, L9
- Gatti M., Shankar F., Bouillot V., Menci N., Lamastra A., Hirschmann M., Fiore F., 2016, *MNRAS*, 456, 1073
- Gatto A., Fraternali F., Read J. I., Marinacci F., Lux H., Walch S., 2013, *MNRAS*, 433, 2749
- Gilli R. et al., 2005, *A&A*, 430, 811
- Grcevich J., Putman M. E., 2009, *ApJ*, 696, 385
- Hand N. et al., 2015, *Phys. Rev. D*, 91, 062001
- Helgason K., Cappelluti N., Hasinger G., Kashlinsky A., Ricotti M., 2014, *ApJ*, 785, 38
- Hivon E., Górski K. M., Netterfield C. B., Crill B. P., Prunet S., Hansen F., 2002, *ApJ*, 567, 2
- Hurier G., Douspis M., Aghanim N., Pointecouteau E., Diego J. M., Macias-Perez J. F., 2015, *A&A*, 576, A90
- Iqbal A., Majumdar S., Nath B. B., Etti S., Eckert D., Malik M. A., 2016, preprint (arXiv:1606.00014)
- Jones C., Forman W., 1984, *ApJ*, 276, 38
- Kereš D., Katz N., Weinberg D. H., Davé R., 2005, *MNRAS*, 363, 2
- Kilbinger M., 2015, *Reports on Progress in Physics*, 78, 086901
- Kim M., Wilkes B. J., Kim D.-W., Green P. J., Barkhouse W. A., Lee M. G., Silverman J. D., Tananbaum H. D., 2007, *ApJ*, 659, 29
- Kolodzig A., Gilfanov M., Hütsi G., Sunyaev R., 2013a, *A&A*, 558, A90
- Kolodzig A., Gilfanov M., Sunyaev R., Sazonov S., Brusa M., 2013b, *A&A*, 558, A89
- Kormendy J., Richstone D., 1995, *ARA&A*, 33, 581
- Koutoulidis L., Plionis M., Georgantopoulos I., Fanidakis N., 2013, *MNRAS*, 428, 1382
- Krumpe M., Miyaji T., Coil A. L., Aceves H., 2012, *ApJ*, 746, 1
- La Barbera F., de Carvalho R. R., de la Rosa I. G., Sorrentino G., Gal R. R., Kohl-Moreira J. L., 2009, *AJ*, 137, 3942
- Leauthaud A. et al., 2015, *MNRAS*, 446, 1874
- Lehmann I. et al., 2001, *A&A*, 371, 833
- LSST Science Collaboration et al., 2009, preprint (arXiv:0912.0201)
- Ma Y.-Z., Van Waerbeke L., Hinshaw G., Hojjati A., Scott D., Zuntz J., 2015, *J. Cosmology Astropart. Phys.*, 9, 46
- Mateos S. et al., 2008, *A&A*, 492, 51
- McCarthy I. G. et al., 2010, *MNRAS*, 406, 822
- McNamara B. R., Nulsen P. E. J., 2007, *ARA&A*, 45, 117
- Merloni A. et al., 2012, preprint (arxiv:1209.3114)
- Miyaji T., Hasinger G., Schmidt M., 2000, *A&A*, 353, 25
- Miyaji T., Krumpke M., Coil A. L., Aceves H., 2011, *ApJ*, 726, 83
- Mo H., van den Bosch F. C., White S., 2010, *Galaxy Formation and Evolution*. Cambridge Univ. Press, Cambridge
- Mo H. J., Mao S., White S. D. M., 1998, *MNRAS*, 295, 319
- Molinari D., Gruppuso A., Polenta G., Burigana C., De Rosa A., Natoli P., Finelli F., Paci F., 2014, *MNRAS*, 440, 957
- Mountrichas G. et al., 2013, *MNRAS*, 430, 661
- Navarro J. F., Frenk C. S., White S. D. M., 1997, *ApJ*, 490, 493
- Omma H., Binney J., Bryan G., Slyz A., 2004, *MNRAS*, 348, 1105
- Oukbir J., Bartlett J. G., Blanchard A., 1997, *A&A*, 320, 365
- Planck Collaboration et al., 2016, *A&A*, 594, A13
- Puchwein E., Sijacki D., Springel V., 2008, *ApJ*, 687, L53
- Putman M. E., Peek J. E. G., Joung M. R., 2012, *ARA&A*, 50, 491
- Refregier A., 2003, *ARA&A*, 41, 645
- Reichert G., Mason K. O., Charles P. A., Bowyer S., Lea S. M., Pravdo S., 1981, *ApJ*, 247, 803
- Richardson J., Chatterjee S., Zheng Z., Myers A. D., Hickox R., 2013, *ApJ*, 774, 143 (R13)
- Sharma M., Nath B. B., 2013, *ApJ*, 763, 17
- Singh P., Majumdar S., Nath B. B., Refregier A., Silk J., 2016, *MNRAS*, 456, 1495
- Singh P., Nath B. B., Majumdar S., Silk J., 2015, *MNRAS*, 448, 2384
- Soltan A. M., 2007, *A&A*, 475, 837
- Springel V., Di Matteo T., Hernquist L., 2005, *MNRAS*, 361, 776
- Takada M., Bridle S., 2007, *New Journal of Physics*, 9, 446
- Tinker J. L., Weinberg D. H., Zheng Z., Zehavi I., 2005, *ApJ*, 631, 41
- Valageas P., Silk J., 1999, *A&A*, 350, 725

- van den Bosch F. C., More S., Cacciato M., Mo H., Yang X.,
2013, MNRAS, 430, 725
Van Waerbeke L., Hinshaw G., Murray N., 2014, Phys. Rev. D,
89, 023508
White M. et al., 2012, MNRAS, 424, 933
Zheng Z., Zehavi I., Eisenstein D. J., Weinberg D. H., Jing Y. P.,
2009, ApJ, 707, 554